



Article

Analysis of the Dissolution of CH₄/CO₂-Mixtures into Liquid Water and the Subsequent Hydrate Formation via In Situ Raman Spectroscopy

Zheng Li ^{1,2} , Christine C. Holzammer ^{1,3} and Andreas S. Braeuer ^{1,*} 

¹ Institute of Thermal-, Environmental-, and Resources' Process Engineering (ITUN), Technische Universität Bergakademie Freiberg (TUBAF), 09599 Freiberg, Germany; zheng.li@cqu.edu.cn (Z.L.); Holzammer.Christine@gmail.com (C.C.H.)

² School of Energy and Power Engineering, Chongqing University, Chongqing 400044, China

³ Erlangen Graduate School in Advanced Optical Technologies (SAOT), Friedrich-Alexander-Universität Erlangen-Nürnberg (FAU), Paul-Gordan-Str. 6, 91052 Erlangen, Germany

* Correspondence: Andreas.Braeuer@tu-freiberg.de; Tel.: +49-3731-392232

Received: 18 December 2019; Accepted: 6 February 2020; Published: 11 February 2020



Abstract: We report an experimental study for the investigation into the suitability of hydrate formation processes for the purification of methane (CH₄) from carbon dioxide (CO₂) at a sub-cooling temperature of 6 K and a pressure of 4 MPa. The experiments were conducted in a stirred batch reactor. Three different initial CH₄/CO₂ mixtures with methane fractions of 70.1 mol%, 50.3 mol%, and 28.5 mol% were tested. The separation efficiency was quantified by measuring in situ via Raman spectroscopy the ratios of CH₄/CO₂ in the gas mixture, the liquid water-rich phase before hydrate formation, and the solid hydrate phase after the onset of the hydrate formation. The results indicated that the main separation effect is obtained due to the preferential dissolution of CO₂ into the liquid water-rich phase before the onset of the hydrate formation.

Keywords: gas hydrates; *in situ* Raman spectroscopy; molar ratio; carbon dioxide; methane

1. Introduction

Gas hydrates are solid crystalline compounds consisting of hydrogen bonded water networks in which guest molecules such as methane (CH₄) and carbon dioxide (CO₂) can be incorporated [1,2]. The guest molecules thermodynamically stabilize the cage-like hydrate crystals. Gas hydrates form at high pressures and low temperatures, with three common hydrate structures existing in nature, known as sI, sII, and sH [3,4]. Natural gas hydrates represent a huge energy resource [5,6]. Synthetic gas hydrates can be utilized for gas storage, gas transportation [7,8], desalination [9,10], gas separation [11–13], etc. Nonetheless, in the case of gas conveyance through pipelines the formation of gas hydrates must be inhibited in order to prevent blockage [14,15].

The formation of gas hydrates from CH₄/CO₂-mixtures has been extensively studied over the past three decades [16–19]. Some works report on the kinetics and selectivity of the gas hydrate formation process [20,21]. In some studies, liquid nitrogen [22] or coolant circulation [23] combined with gas chromatography were utilized for measuring gas compositions in a solid phase. Existing studies usually neglect the amount of CH₄ and CO₂ dissolved in the liquid water-rich phase, which after hydrate formation usually coexists with the solid hydrate phase. Holzammer et al. found that synthetically formed gas hydrates are rather gels or slurries that contain significant inclusions of a liquid water-rich phase. The fraction of the pure solid hydrate in these hydrate slurries or gels was found to be less than 30 wt.-% [24,25]. Therefore, the assumption that all the gas which is missing in the gaseous phase after the hydrate formation must have been incorporated in the formed pure solid

hydrate phase is prone to error, especially if the solubility of the gas species in the liquid water-rich phase, which coexists with the hydrate phase, is high. To the knowledge of the authors, there has been no study that correlates the composition of the CH_4/CO_2 gas mixture, with the dissolution of CH_4 and CO_2 into the liquid water-rich phase before the hydrate formation and the subsequent incorporation of CH_4 and CO_2 into the solid gas hydrate phase.

Raman spectroscopy is one possible method for the remote and *in situ* measurement of the composition of fluid and solid mixtures and has been applied to the analysis of gas hydrates and fluid mixtures in the context of gas hydrates [26,27].

Therefore, the object of this work is to put into context the composition of the gaseous CH_4/CO_2 -mixture with the dissolution of CH_4 and CO_2 into the liquid water-rich phase before hydrate formation and the incorporation of CH_4 and CO_2 into the solid pure hydrate phase using Raman spectroscopy. Three different initial gas compositions were employed to evaluate the effect of the initial gas composition on the fractions of CH_4 and CO_2 in the vapor phase, the liquid water-rich phase, and the hydrate phase. Finally, CO_2 selectivities relevant for gas separation or gas purification processes are discussed.

2. Materials and Methods

2.1. Materials

The experiments were conducted with deionized water with a conductivity of less than $10 \mu\text{S}/\text{cm}$ and with gaseous premixed binary CH_4/CO_2 -mixtures (Linde, molar purity 99.5%) with three certificated CH_4 molar fractions of 0.701, 0.503, and 0.285.

2.2. Apparatus

A schematic diagram of the experimental setup is given in Figure 1, which consists of a high-pressure view cell (maximum pressure 25 MPa, internal and non-adjustable volume 26 mL) and a Raman probe.

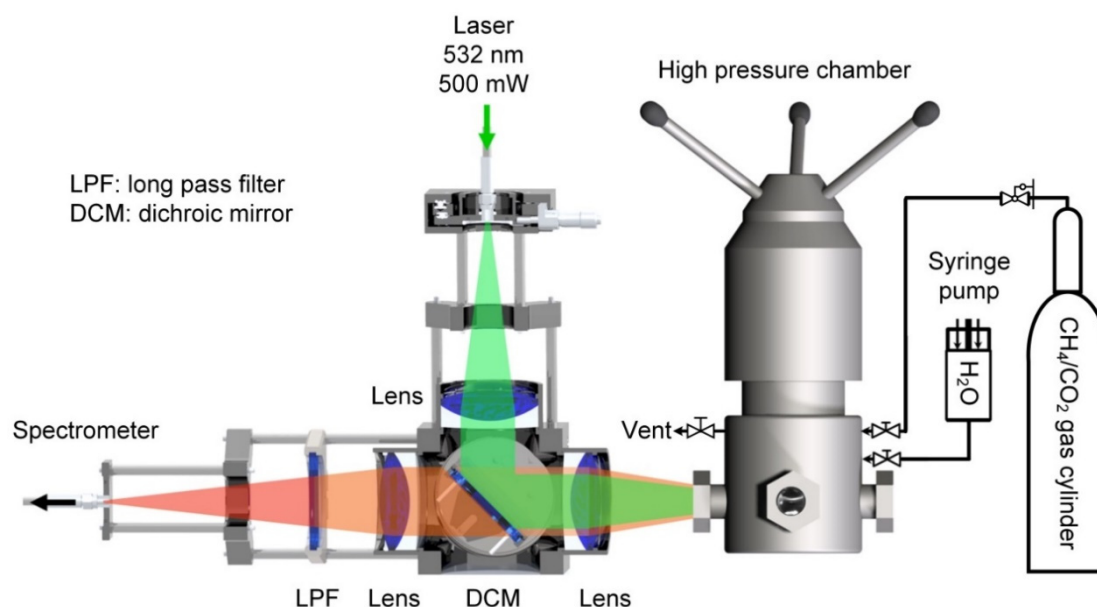


Figure 1. Sketch of the experimental setup, including the high pressure view cell.

The high-pressure view cell is equipped with four optical windows. Two of them are required for launching the laser through the view cell, which is required for the Raman spectroscopy and for the detection of the Raman signals. The two remaining windows were utilized for the visual observation

of the fluids and solids (gels or slurries) inside the view cell. The temperature of the cell was controlled by a cryo-compact Julabo circulator (model CF41) which pumps conditioned coolant through the double-walled cooling jacket surrounding the view cell. A PT100 temperature sensor (resolution 0.05 K, uncertainty 0.12 K) and a pressure sensor (model PAA-33X, precision 0.01 MPa) from Keller were utilized for monitoring the temperature and pressure in the cell, respectively. The temperature and pressure data were recorded and saved each second by the computer. A high precision Teledyne Isco syringe pump (model 260D) fed well-defined amounts of distilled water into the cell.

A frequency-doubled Nd:YAG laser (model 532-250-AC) from CNI with an emission wavelength of 532.27 nm and a power of 500 mW was utilized as the light source within the Raman spectrometer. The laser beam was guided by an optical fiber to the Raman probe. After collimation by a convex lens, the beam reached a dichroitic mirror (DCM) which reflects light with wavelengths shorter than 533 nm and transmits light with wavelengths longer than 544 nm (the Cut-Off wavelength is in between). Subsequently, the reflected laser light was focused into the view cell through a convex lens (focal length 100 mm). The probe volume can be assumed to have a cylindrical shape approximately 5 mm in length and 0.2 mm in diameter. The laser light was scattered elastically and inelastically from the matter within the probe volume. The inelastically Raman Stokes-scattered light (scattered at wavelengths longer than the laser wavelength) was collected by the lens in the back-scattering direction [28], collimated, and passed straightly through the dichroitic mirror, and then was guided via a lens and an optical fiber toward a spectrometer (QE65 Pro, entrance slit 100 μm , Ocean Optics with a resolution of $\sim 15\text{ cm}^{-1}$). A long-pass filter (LPF) was set behind the dichroitic mirror to remove any remaining elastically scattered light. The signal integration time of each Raman spectrum was 1 s.

2.3. Procedures

All the experiments were performed in a batch manner (with a constant volume of 26 mL). Before each experiment the inner volume of the cell was cleaned and dried. Then, 14 mL of distilled water were injected into the cell through the syringe pump. The air remaining inside the chamber was removed by purging the cell five times with the premixed feed gas mixture composed of CO_2 and CH_4 , still without pressurizing the view cell. The gas inlet and exit valves were situated above the meniscus of liquid water. Then, the cell was closed and cooled to the desired experimental temperature T_{exp} . All the experiments were conducted at a constant initial sub-cooling of 6 K. The sub-cooling (ΔT) for hydrate formation is defined as the temperature difference between the equilibrium temperature (T_{eq}) and the experimental temperature (T_{exp}) at a specific pressure (here 4 MPa). T_{eq} was predicted by CSMHyd program [29]. Thus, T_{exp} for initial CH_4/CO_2 -mixtures with CH_4 molar fractions of 0.701, 0.503, and 0.285 is 274.2 K, 275.3 K, and 276.1 K, respectively. Once the fluids inside the view cell reached the set temperature, the cell was pressurised to a fixed initial pressure p_{ini} of 4 MPa by introducing the premixed CH_4/CO_2 -mixture via a pressure controller slowly from the gas cylinder. The pressurization took less than 10 s. Once the pressure was 4 MPa (instant “time zero” t_0), the gas inlet valve was closed and a magnetic stirrer started to rotate a magnetic stirring bar situated inside the cell at its bottom. The magnetic bar rotated with ~ 400 rotations per minute and accelerated the dissolution of CH_4 and CO_2 from the gas phase into the water-rich phase. The pressure inside the view cell dropped due to the dissolution. The beginning of hydrate formation was indicated by another pressure drop, as additional CH_4 and CO_2 were then removed from the gas phase. At “time zero”, we also started to acquire Raman spectra with a repetition rate of 3 spectra per minute and a signal integration time of 1 s per spectrum. Considering the operational conditions, the molar ratio $n_{\text{H}_2\text{O}}/(n_{\text{CO}_2} + n_{\text{CH}_4})$ fed into the cell is larger than 29. In studies of sI hydrate structures, this ratio is typically close to 6 [30,31]. We chose a rather large ratio in order to obtain a significant change of the composition in the gas phase coexisting with the hydrate slurry/gel.

3. Results

Figure 2 shows as solid line the temporal evolution of the pressure inside the view cell at 276.1 K for the fed gas mixture, with a methane molar fraction of 0.285. The two grey dashed pressure curves represent two repetitions of the same experiment. The pressure curves start at “time zero” t_0 at 4 MPa. Between t_0 and t_1 (instant t_1 only labelled for the solid black curve), the pressure drops due to the dissolution of CH_4 and CO_2 into the liquid water-rich phase. This period is denoted as the gas dissolution period. At instant t_1 , the pressure curve features a kink indicating the start of hydrate formation. Due to the exothermic nature of the hydrate formation, this pressure kink is accompanied by a temperature spike of approximately 0.5 K towards higher temperatures. Subsequently, the pressure decreases further owing to the growth of the hydrate phase which consumes further gas. The experiment is kept running until the pressure decrease is less than 0.01 MPa per hour. The period between the onset of the hydrate formation t_1 and the end t_2 of the experiment ($t_2 - t_1 \geq 20$ h) is called the hydrate formation period. This does not imply that no gas dissolves into the liquid water-rich phase during the period of hydrate formation. The pressure 2.13 MPa reached at t_2 is close to the pressure of 2.2 MPa expected for thermodynamic equilibrium according to the software CSMHyd, developed by the hydrate research center of the Colorado School of Mines. The hydrate layer formed at the interface to the gaseous phase acts as mass transfer resistance and can kinetically limit further hydrate growth and, along with this, also limit the pressure drop towards t_2 . From the pressure decrease in the dissolution period (before t_1) and in the hydrate formation period (after t_1), one can already conclude that the dissolution period alone extracts a significant amount of CH_4 and/or CO_2 from the vapor phase. At the end of the experiment, the cell is depressurized, emptied, and cleaned for the next experiment. The experiments are repeated with the aforementioned procedure a minimum of three times for each initial composition of the CH_4/CO_2 mixture. Figure 2 also shows that the position of the Raman probe volume (laser focus beam waist) is fixed either in the vapor phase or just below the gas/liquid or gas/hydrate gel interface. Unfortunately, as there was only one Raman probe available, we were not able to simultaneously make Raman measurements above and below the interface. Therefore, serial experiments had to be conducted to obtain the Raman spectra from different phases at the same experimental condition.

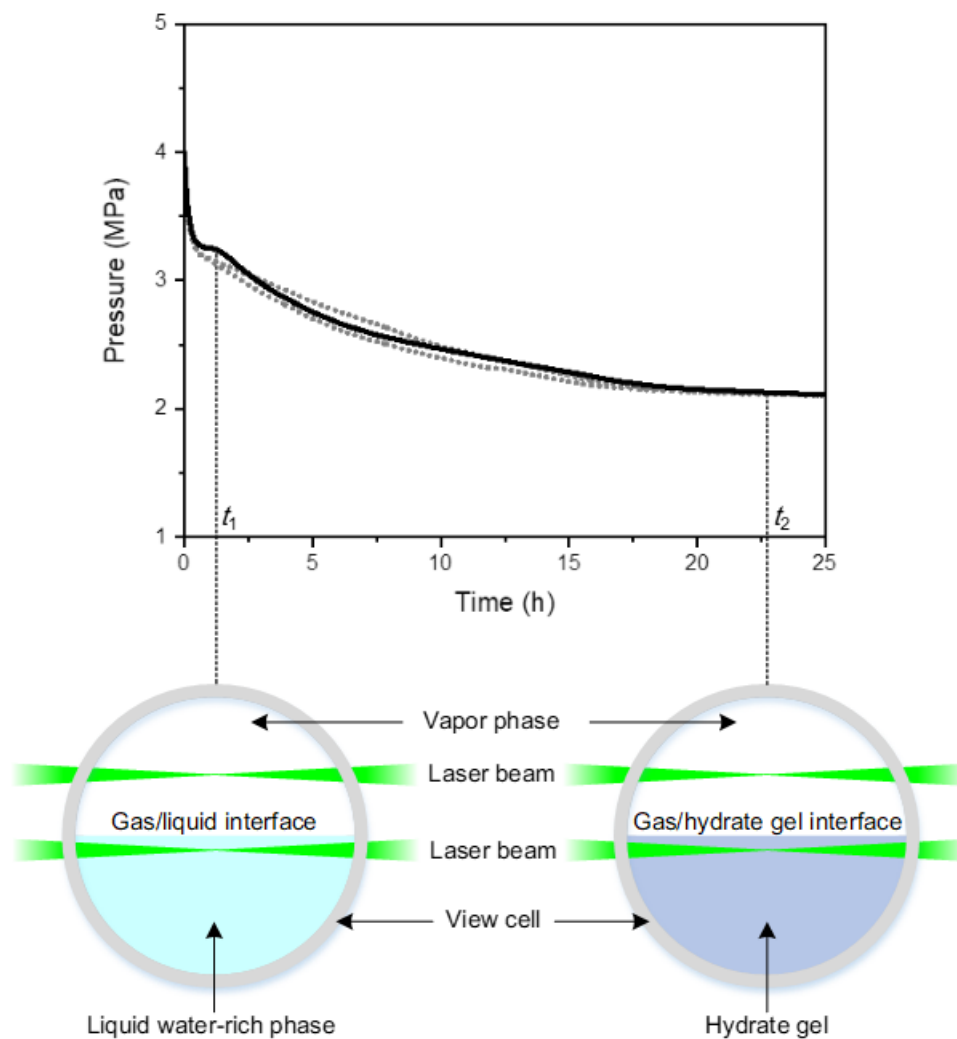


Figure 2. The temporal evolution of the pressure inside the view cell before and during the hydrate formation. The solid black line pressure profile represents an independent experiment, in which t_1 denotes the onset of the hydrate formation and t_2 the end of the hydrate formation period. The two grey dashed pressure curves represent two repetitions of the same experiment. Sketches are provided for two instants inside the view cell. The green lines indicate the path of the laser beam for composition measurements in the gaseous, liquid, and gel phases. Temperature $T = 276.1$ K.

3.1. Raman Spectra of CH_4/CO_2 -Mixtures in Vapor Phase, Liquid Water-rich Phase, and Hydrate Gel Phase

Figure 3 shows typical Raman spectra of pure water before pressurization, the liquid water-rich phase after pressurization but before the hydrate formation, hydrate gel at the end of the experiment (t_2), and the vapor phase at t_0 , all at 276.1 K. The CH_4 molar fraction in the feed gas mixture is 0.285. These Raman spectra are baseline corrected and normalized to their maximum.

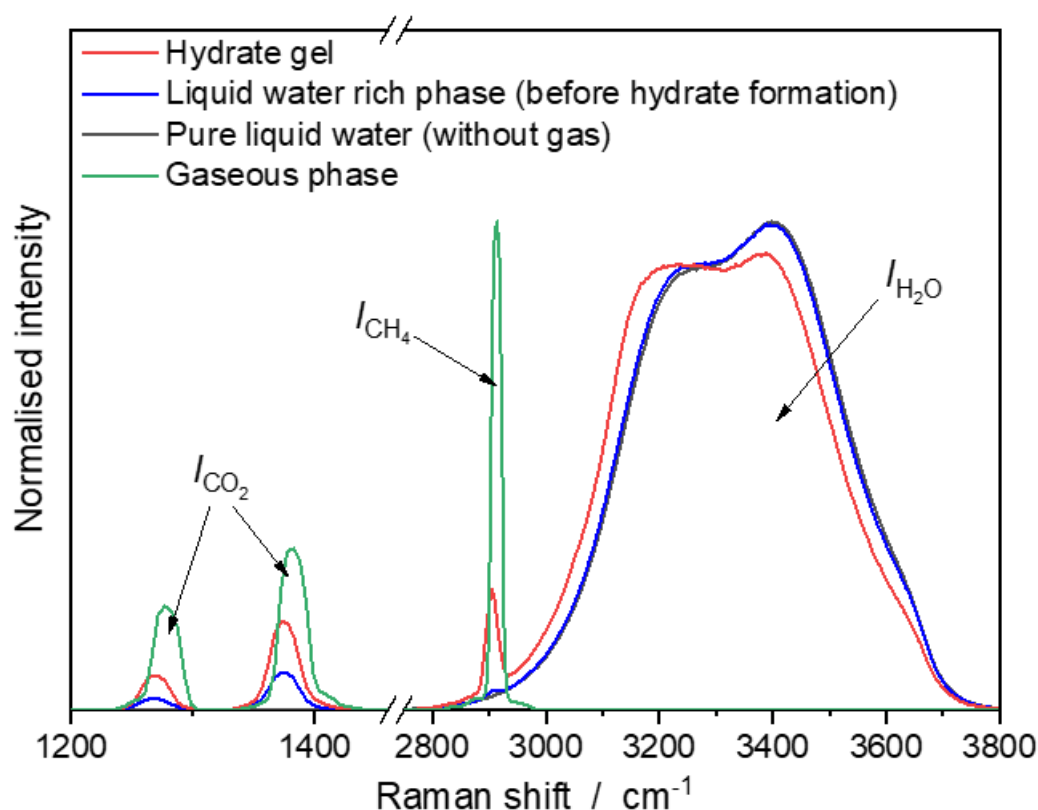


Figure 3. Example Raman spectra of the liquid water-rich phase at instant t_1 (see Figure 2), the hydrate gel at instant t_2 (see Figure 2), the gaseous CH_4/CO_2 -mixture at instant t_0 (see Figure 2), and pure liquid water at $T = 276.1$ K. (For the pure liquid water spectrum, the pressure is $p = 0.1$ MPa).

The double peak structure, the so-called Fermi Dyad [32], at 1280 cm^{-1} and 1380 cm^{-1} , is assignable to the CO_2 species (additional CO_2 peaks merged with the CO_2 Fermi Dyad, due to the resolution of the spectrometer). The peak centered at 2910 cm^{-1} is assignable to the C–H vibration between carbon and hydrogen nuclei and is thus assignable to the CH_4 species. The broad band between 2800 cm^{-1} and 3800 cm^{-1} is assignable to the symmetric stretching vibration of the H_2O species in the liquid or the solid form. The broadband nature of the symmetric stretching vibration of condensed water is due to the existence of a hydrogen bonded network [33–35]. It is well known that the temperature, density, amount of substance of dissolved compounds, as well as the state of the water affect the development of the hydrogen bonded network and, with this, the shape of the respective broad Raman band. The hardly visible marginal differences between the Raman band of pure water (black in Figure 3) before pressurization and the water-rich solution after pressurization (blue in Figure 3) with the gas mixture is due to the dissolved CO_2 and CH_4 that disturb the hydrogen bonded network. The presence of CH_4 and CO_2 in the water-rich liquid phase can be extracted from the existence of the CO_2 - and CH_4 -characteristic Raman peaks in its spectrum. The Raman spectrum measured from the hydrate gel (red in Figure 3) features a symmetric water stretching band that is significantly different to the Raman spectra of pure water and the water-rich liquid phase at the same temperature. This significant alteration is due to the existence of solid hydrate in the gel, whereby the hydrogen bonded network is much more developed in the solid hydrate than it is in the liquid water. As a consequence, the left shoulder of the broad water stretching vibration band grows in relation to its right shoulder.

Furthermore, it can be seen that the center peak positions of CO_2 and CH_4 are influenced by the state of phase. When CO_2 or CH_4 are dissolved in a liquid water-rich phase or incorporated in the cage structure of hydrates, their intramolecular vibrations are influenced by their environment, which causes a peak shift towards smaller Raman shifts.

The ratio of various peak intensities $\frac{I_{\text{CH}_4}}{I_{\text{CO}_2}}$ within one Raman spectrum:

$$\frac{I_{\text{CH}_4}}{I_{\text{CO}_2}} = \alpha \frac{n_{\text{CH}_4}}{n_{\text{CO}_2}} \quad (1)$$

is directly proportional to the ratio of the amount of the respective substances $\frac{n_{\text{CH}_4}}{n_{\text{CO}_2}}$, with α being the proportionality constant. The intensity I of a peak is computed by fitting model peaks (Gaussian, Lorentzian, or quasi-Voigt profile shapes), as described by Schuster et al. [36] and as frequently applied in the widely spread “Indirect hard modelling” approach [37,38]. Then, the intensity I of the modelled peaks is determined by their integration and taken as the intensity of the real peak.

In order to find the proportionality factor α which is relevant for the applied Raman spectroscopic sensor, we made calibration measurements in each of the available gas mixtures.

Figure 4 shows the correlation of the Raman signal intensity ratio $\frac{I_{\text{CH}_4}}{I_{\text{CO}_2}}$ and the molar ratio $\frac{n_{\text{CH}_4}}{n_{\text{CO}_2}}$ in the gaseous binary CH_4/CO_2 -mixtures. For each composition, ten measurements were repeated. The error bars (see Figure 4) represent the standard deviation of ten repetitions. It has been shown several times that the ratio calibration method is not affected by the state of phase [39,40]. Therefore, a ratio-calibration that has been performed in gaseous mixtures can also be applied to liquids, supercritical fluids, gels, or solids.

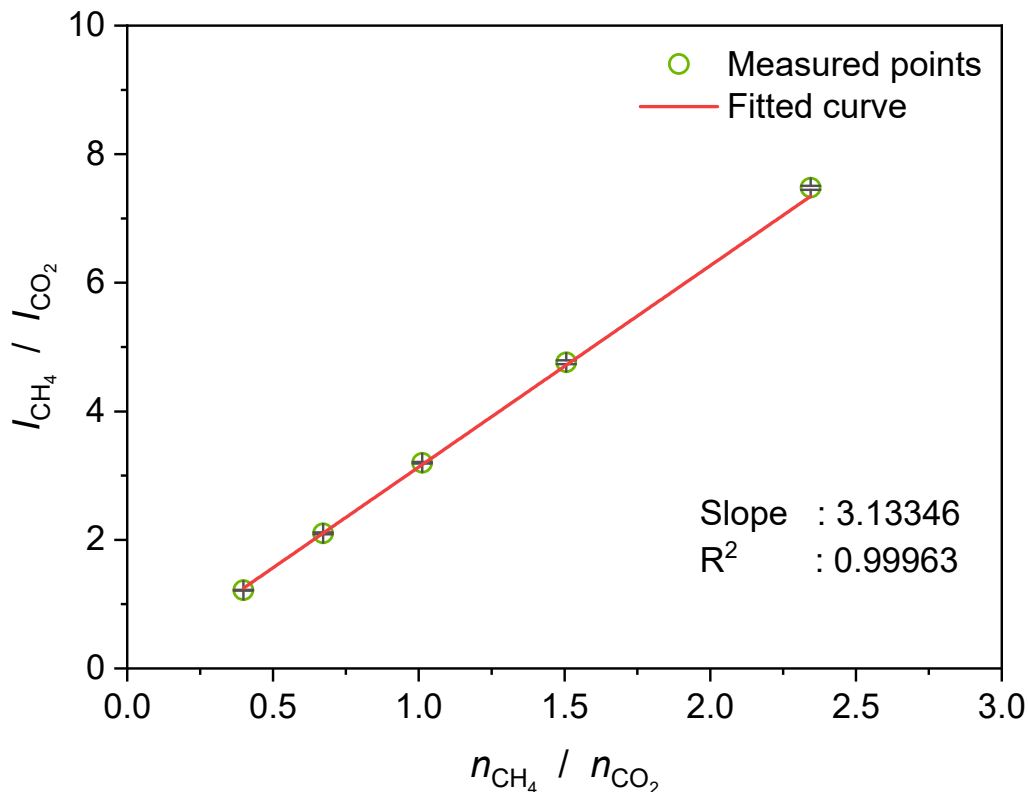


Figure 4. The correlation of the Raman signal intensity ratio $\frac{I_{\text{CH}_4}}{I_{\text{CO}_2}}$ and the amount of substance ratio $\frac{n_{\text{CH}_4}}{n_{\text{CO}_2}}$ in the gaseous binary CH_4/CO_2 -mixture.

3.2. Effect of Feed Gas Composition on the Evolution of $\frac{n_{\text{CH}_4}^V}{n_{\text{CO}_2}^V}$ in the Vapor Phase

The temporal evolution of the molar ratio of CH_4 and CO_2 in the vapor phase $\frac{n_{\text{CH}_4}^V}{n_{\text{CO}_2}^V}$ is given in Figure 5 for three different initial gas compositions.

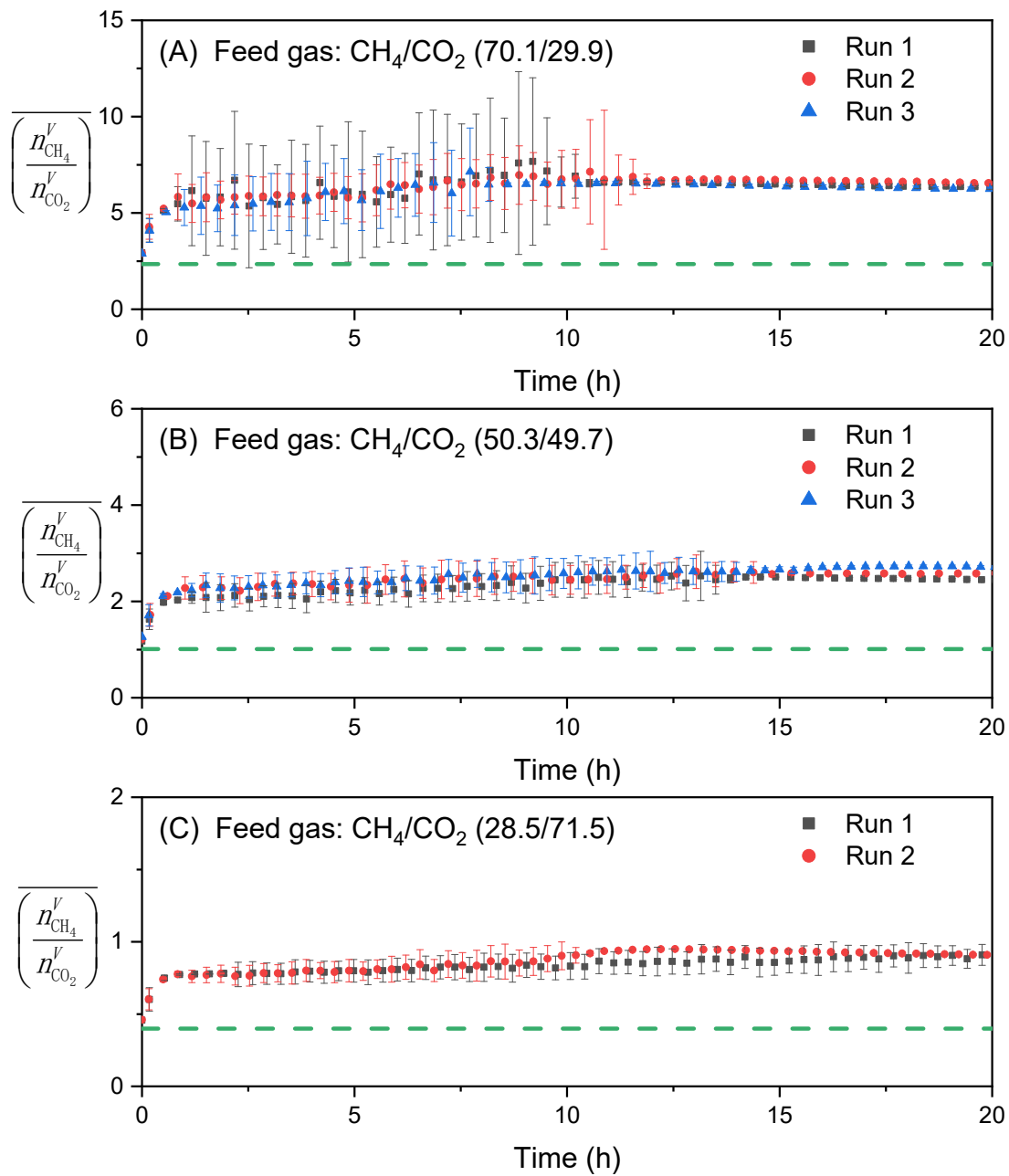


Figure 5. The evolution of the molar ratio $\left(\frac{n_{\text{CH}_4}^V}{n_{\text{CO}_2}^V}\right)$ in the gaseous phase before and during the hydrate formation at $p_{\text{ini}} = 4$ MPa and for three different feed gas compositions: (A) methane fraction 0.701, (B) methane fraction 0.503 and (C) methane fraction 0.285.

The dashed horizontal lines denote the initial $\left(\frac{n_{\text{CH}_4}^V}{n_{\text{CO}_2}^V}\right)^0$ ratio in the feed gas for reference. The colored data points represent mean $\left(\frac{n_{\text{CH}_4}^V}{n_{\text{CO}_2}^V}\right)$ values that were averaged from 60 subsequently measured $\frac{n_{\text{CH}_4}^V}{n_{\text{CO}_2}^V}$ values (corresponds to a measurement time of 20 min times 3 spectra per minute). The error bars represent the standard deviation of these 60 measurements. Considering the averaged values together with their standard deviation enables the illustration of several experimental runs in one diagram, as without averaging the diagrams would be overloaded with data points. Each data point train corresponds to one experimental run.

The transition from the dissolution period to the hydrate growth period at time t_1 is not extractable (no obvious kink) from the evolutions of $\left(\frac{n_{\text{CH}_4}^V}{n_{\text{CO}_2}^V}\right)$ in the vapor phase, but can be extracted from the temporal pressure profile, as described in the context of Figure 2. It can be seen from Figure 5 that $\left(\frac{n_{\text{CH}_4}^V}{n_{\text{CO}_2}^V}\right)$ at $t_0 = 0$ h is always larger than that of the feed gas. This is due to averaging values with an overall increasing tendency (positive slope) and due to the dissolution of CH_4 and CO_2 into the liquid water-rich phase already before t_0 during the pressurization process. $\left(\frac{n_{\text{CH}_4}^V}{n_{\text{CO}_2}^V}\right)$ increases rapidly within the first 60 min after t_0 and slower at later times after t_1 . The significant variation of $\left(\frac{n_{\text{CH}_4}^V}{n_{\text{CO}_2}^V}\right)$ must therefore be assigned to the dissolution of CO_2 and CH_4 into the liquid water-rich phase. The gas dissolution period contributes approximately $72.1\% \pm 0.8\%$, $71.4\% \pm 1.0\%$, and $71.8\% \pm 3.9\%$ to the total increase of $\left(\frac{n_{\text{CH}_4}^V}{n_{\text{CO}_2}^V}\right)$, respectively. The ratio $\left(\frac{n_{\text{CH}_4}^V}{n_{\text{CO}_2}^V}\right)$ can only increase, if at the same time the ratio $\left(\frac{n_{\text{CH}_4}^L}{n_{\text{CO}_2}^L}\right)$ of the amount of substances of CH_4 and CO_2 dissolved in the liquid water-rich phase is smaller than $\left(\frac{n_{\text{CH}_4}^V}{n_{\text{CO}_2}^V}\right)$. At the end of the experiment at t_2 , $\left(\frac{n_{\text{CH}_4}^V}{n_{\text{CO}_2}^V}\right)$ is approximately 2.66 ± 0.08 , 2.55 ± 0.13 , and 2.31 ± 0.10 times that in the initial feed gas, with methane molar fractions in the feed gas of 0.701, 0.503, and 0.285, respectively.

It is obvious that the error bars are small during the dissolution period, are then first large during the early phase of the hydrate formation period, before later decreasing again. During the early phase of hydrate formation and due to the intensive agitation of the system, liquid water-rich ligaments might precipitate on the windows of the cell or be dispersed into the gaseous phase. These ligaments can convert to hydrate gels and deflect the laser beam or, if they appear close to the probe volume, cause an interference of the desired Raman signals from the gaseous phase and the undesired Raman spectra detected from the ligaments. Once a coherent hydrate gel layer has formed at the interface to the gaseous CO_2/CH_4 -mixture, no more liquid-rich ligaments can be dispersed into the gaseous phase, and thus the error bars become smaller.

3.3. Effect of Feed Gas Composition on the Molar Fraction of Hydrate x^H in the Hydrate Gel Phase

As mentioned above, the hydrate gel (superscript G) is composed of pure solid gas hydrate (superscript H) with inclusions of a liquid water-rich phase (superscript L). In order to separate the fraction of water contained in the pure solid hydrate $x_{\text{H}_2\text{O}}^H$ from the fraction of water contained in the included liquid water-rich phase $x_{\text{H}_2\text{O}}^L$ with

$$x_{\text{H}_2\text{O}}^H = \frac{n_{\text{H}_2\text{O}}^H}{n_{\text{H}_2\text{O}}^H + n_{\text{H}_2\text{O}}^L} \ \& \ x_{\text{H}_2\text{O}}^H + x_{\text{H}_2\text{O}}^L = 1 \quad (2)$$

we follow exactly the approach reported by Holzammer et al. [25]. In short, this approach is based on the deconstruction of the broad water stretching vibration Raman band $I_{\text{H}_2\text{O}}^G$ of the gel into contributions assignable to the pure hydrate $I_{\text{H}_2\text{O}}^H$ and assignable to the included liquid water-rich phase $I_{\text{H}_2\text{O}}^L$.

Figure 6 shows the temporal evolution of the fraction of water contained in the hydrate phase $x_{\text{H}_2\text{O}}^H$ for three initial feed gas compositions. t_1 is defined by the first data point shown for each experimental run. In general, the curve shapes of the temporal evolutions of $x_{\text{H}_2\text{O}}^H$ are similar to the ones reported by Holzammer et al. [24], but with a deviating final $x_{\text{H}_2\text{O}}^H$. The smallest $x_{\text{H}_2\text{O}}^H$ (0.2434 ± 0.0068) is obtained from the CH_4/CO_2 -mixture with a molar CH_4 -fraction of 0.701, which is quite similar to the literature

data (0.216) published by Di Profio et al. [41] in a stirred tank reactor at the same initial pressure of 4 MPa and at a temperature of 274 K with a similar molar CH_4 fraction of 0.6.

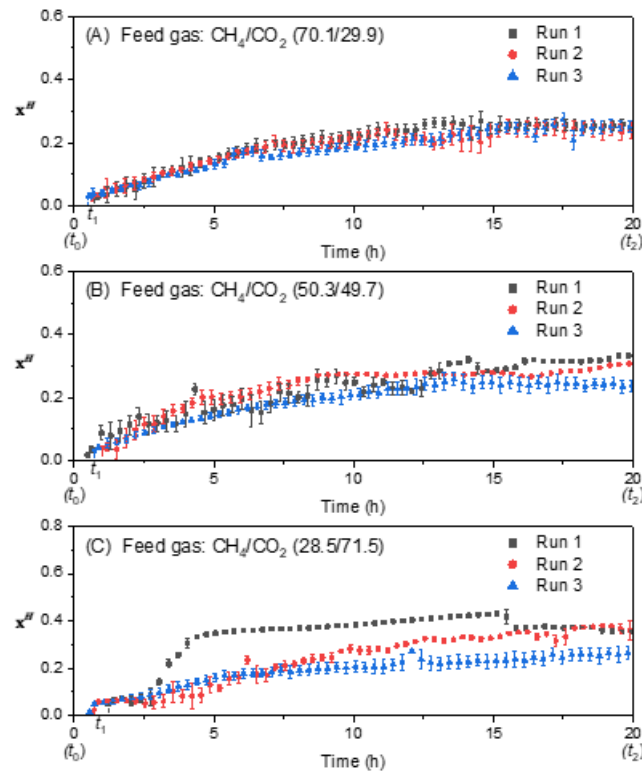


Figure 6. The evolution of the fraction of hydrate x^H contained within the gel for three different gas compositions. (A) feed gas methane fraction 0.701, (B) feed gas methane fraction 0.503 and (C) feed gas methane fraction 0.285.

3.4. Effect of Feed Gas Composition on the Evolution of the Molar Ratio $\frac{n_{\text{CH}_4}}{n_{\text{CO}_2}}$ in the Liquid Water-Rich Phase

$\frac{n_{\text{CH}_4}^L}{n_{\text{CO}_2}^L}$ and in the Solid Hydrate Phase $\left(\frac{n_{\text{CH}_4}^H}{n_{\text{CO}_2}^H}\right)$

Before hydrate formation (before t_1), the molar ratio $\frac{n_{\text{CH}_4}^L}{n_{\text{CO}_2}^L}$ of CH_4 and CO_2 dissolved in the liquid water-rich phase can be computed from:

$$\frac{I_{\text{CH}_4}^L}{I_{\text{CO}_2}^L} = \alpha \frac{n_{\text{CH}_4}^L}{n_{\text{CO}_2}^L} \quad (3)$$

the ratio of the Raman signal intensities of $I_{\text{CH}_4}^L$ and $I_{\text{CO}_2}^L$ with $\alpha = 3.13346$ being the proportionality constant derived during the calibration in various CH_4/CO_2 mixtures (see Figure 4). Both $I_{\text{CH}_4}^L$ and $I_{\text{CO}_2}^L$ are extractable from the Raman spectra recorded from the water-rich liquid phase. Figure 7 shows the evolution of $\frac{n_{\text{CH}_4}^L}{n_{\text{CO}_2}^L}$ in the liquid water-rich phase before t_1 (before the hydrate formation). The number of data points per data row vary as the start of the hydrate formation, which is indicated by the kink in the pressure profile, stochastically varies from experiment to experiment. At early times in the dissolution period, the ratios $\frac{n_{\text{CH}_4}^L}{n_{\text{CO}_2}^L}$ are small, meaning that significantly more CO_2 than CH_4 is dissolved into the liquid water-rich phase. Combining this derivation (Figure 7) with the significant pressure decrease obtained especially also at early times in the dissolution period (Figure 2), one can

conclude that the overall change of the vapor phase ratio $\left(\frac{n_{CH_4}^V}{n_{CO_2}^V}\right)$ largely depends on the early times of the dissolution period. With decreasing initial $\left(\frac{n_{CH_4}^V}{n_{CO_2}^V}\right)^0$ in the vapor phase, the ratio $\frac{n_{CH_4}^L}{n_{CO_2}^L}$ in the liquid water-rich phase decreases significantly.

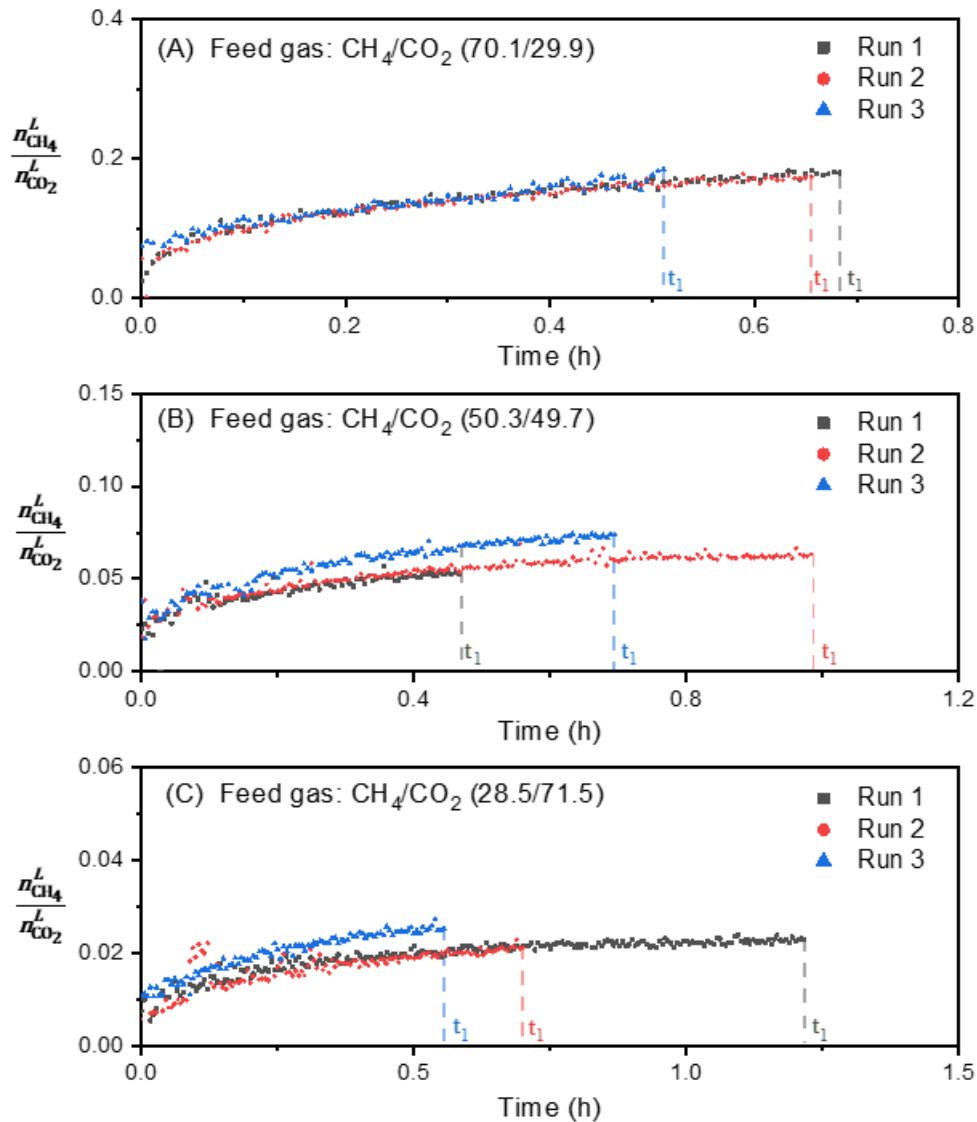


Figure 7. The evolution of the molar ratio $\frac{n_{CH_4}^L}{n_{CO_2}^L}$ in the liquid water-rich phase (before hydrate formation) at $P_{ini} = 4$ MPa and for three different initial gas compositions. (A) feed gas methane fraction 0.701, (B) feed gas methane fraction 0.503 and (C) feed gas methane fraction 0.285.

After hydrate formation, the Raman signals coming from the liquid water-rich phase and from the hydrate phase interfere with each other and together form the Raman signal coming from the hydrate gel. In order to be able to compute the molar ratio $\frac{n_{CH_4}^H}{n_{CO_2}^H}$ of CH_4 to CO_2 contained in the pure solid hydrate without the interference from the liquid water-rich phase, we follow the approach by Holzammer et al. [25]. First, we deconstruct the Raman spectrum of the hydrate gel into the intensity contributions assignable to water in the liquid state $I_{H_2O}^L$, water in the hydrate state $I_{H_2O}^H$, CH_4 in the gel $I_{CH_4}^G$, and CO_2 in the gel $I_{CO_2}^G$. These quantities can be extracted directly from the acquired Raman spectra and are written in bold in the following equations.

The Raman signal intensity $I_{CH_4}^G$ of CH_4 in the gel is simply the summation of the CH_4 Raman signal intensities coming from the hydrate $I_{CH_4}^H$ and the liquid phase $I_{CH_4}^L$. The same is true for H_2O and for CO_2 . Therefore the ratio

$$\frac{I_{CH_4}^G}{I_{H_2O}^G} = \frac{I_{CH_4}^H + I_{CH_4}^L}{I_{H_2O}^H + I_{H_2O}^L} = \frac{\frac{I_{CH_4}^H}{I_{H_2O}^H}}{1 + \frac{I_{H_2O}^L}{I_{H_2O}^H}} + \frac{\frac{I_{CH_4}^L}{I_{H_2O}^L}}{1 + \frac{I_{H_2O}^L}{I_{H_2O}^H}} \quad (4)$$

can be expressed by various other ratios. Assuming that the solubility of CH_4 in the liquid water-rich phase remains constant during the hydrate formation after t_1 , the ratio $\frac{I_{CH_4}^L}{I_{H_2O}^L}$ can be extracted from the Raman spectrum recorded just before hydrate formation (just before t_1). Thus, $\frac{I_{CH_4}^L}{I_{H_2O}^L}$ is also known and in the following is also represented in bold. Consequently, we transform the equation above and obtain an equation for the computation of

$$\frac{I_{CH_4}^H}{I_{H_2O}^H} = \left(\frac{I_{CH_4}^G}{I_{H_2O}^G} - \frac{\frac{I_{CH_4}^L}{I_{H_2O}^L}}{1 + \frac{I_{H_2O}^L}{I_{H_2O}^H}} \right) \left(1 + \frac{I_{H_2O}^L}{I_{H_2O}^H} \right) \quad (5)$$

What has been shown above for CH_4 can be repeated in an identical manner for CO_2 , from which

$$\frac{I_{CO_2}^H}{I_{H_2O}^H} = \left(\frac{I_{CO_2}^G}{I_{H_2O}^G} - \frac{\frac{I_{CO_2}^L}{I_{H_2O}^L}}{1 + \frac{I_{H_2O}^L}{I_{H_2O}^H}} \right) \left(1 + \frac{I_{H_2O}^L}{I_{H_2O}^H} \right) \quad (6)$$

follows. Additionally, here the ratio $\frac{I_{CO_2}^L}{I_{H_2O}^L}$ can be extracted from the last Raman spectrum recorded just before the onset of hydrate formation (just before t_1). In a last step, the ratio of the values we obtained for $\frac{I_{CH_4}^H}{I_{H_2O}^H}$ according to Equation (5) and $\frac{I_{CO_2}^H}{I_{H_2O}^H}$ according to Equation (6),

$$\frac{\frac{I_{CH_4}^H}{I_{H_2O}^H}}{\frac{I_{CO_2}^H}{I_{H_2O}^H}} = \frac{I_{CH_4}^H}{I_{CO_2}^H} = \alpha \frac{n_{CH_4}^H}{n_{CO_2}^H} \quad (7)$$

results in the desired molar ratio $\frac{n_{CH_4}^H}{n_{CO_2}^H}$ of CH_4 and CO_2 in the pure hydrate, where $\alpha = 3.13346$ is the proportionality constant we obtained from the calibration measurements in different gas mixtures (see Figure 2).

Figure 8 shows the temporal evolution of the molar ratio of CH_4 and CO_2 in the pure solid hydrate phase $\left(\frac{n_{CH_4}^H}{n_{CO_2}^H} \right)$ during the hydrate formation for three different initial gas compositions. The first data point of each data row defines the start of the hydrate formation (t_1). The dashed horizontal green lines denote the initial $\left(\frac{n_{CH_4}^V}{n_{CO_2}^V} \right)^0$ ratio in the feed gas for reference. It should be reminded that already after the dissolution period the ratio $\left(\frac{n_{CH_4}^V}{n_{CO_2}^V} \right)$ differs significantly from the initial one (compare Figure 5). The mean final ratios $\left(\frac{n_{CH_4}^V}{n_{CO_2}^V} \right)$ in the vapor phase for t_2 (end of the hydrate formation period) are also provided as reference in Figure 8 (grey horizontal lines). The colored data points represent the mean

$\left(\frac{n_{\text{CH}_4}^H}{n_{\text{CO}_2}^H}\right)$ values that were averaged from the 60 subsequently calculated $\frac{n_{\text{CH}_4}^H}{n_{\text{CO}_2}^H}$ values by Equations (5)–(7). The error bars represent the standard deviation of these 60 calculated values. Each data point train corresponds to one experimental run.

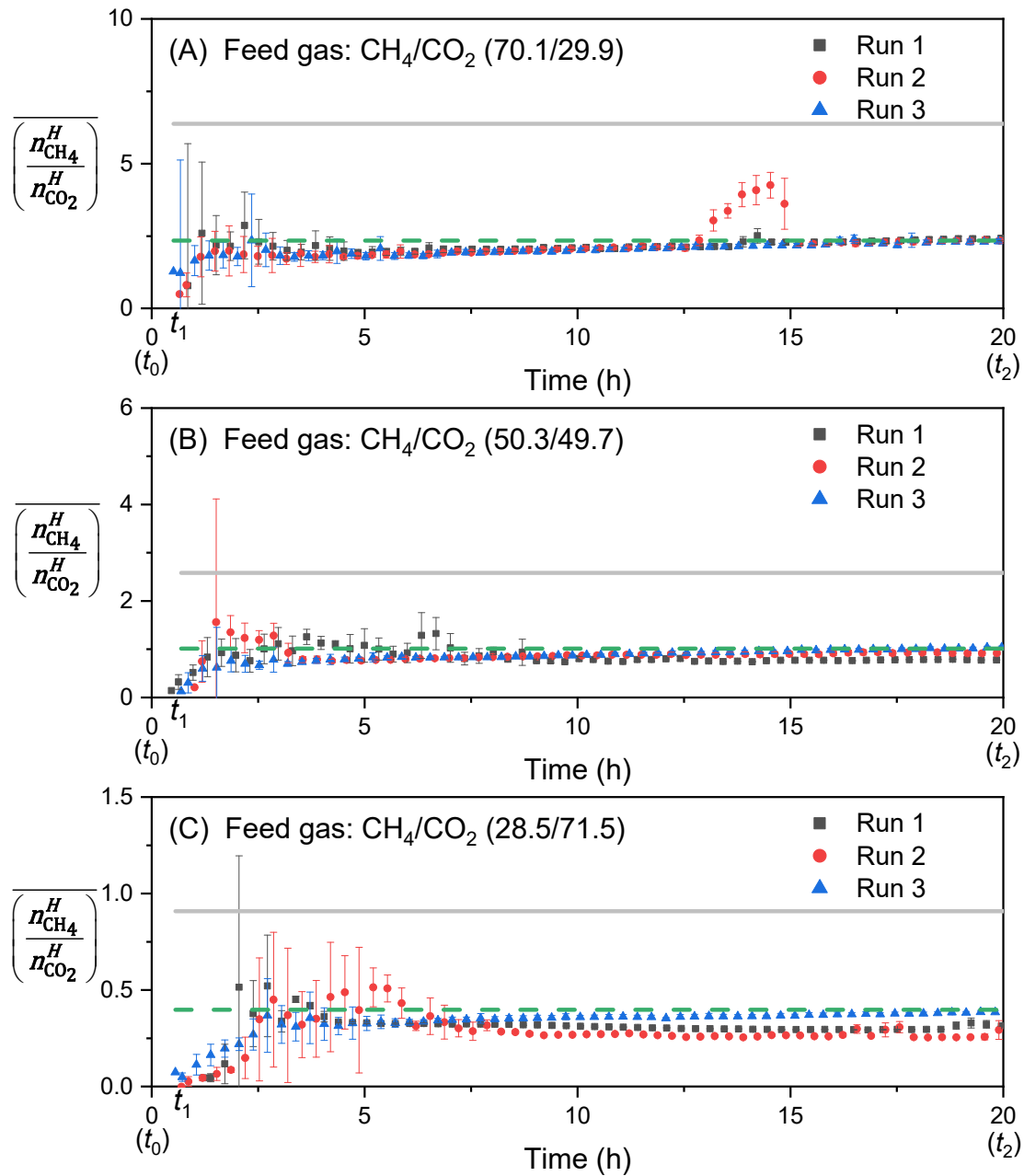


Figure 8. The evolution of the molar ratio $\left(\frac{n_{\text{CH}_4}^H}{n_{\text{CO}_2}^H}\right)$ in the solid hydrate phase in the gel phase during the hydrate formation at $p_{\text{ini}} = 4 \text{ MPa}$ and for three different initial gas compositions. The dashed lines indicate the initial CH_4/CO_2 ratio at t_0 of the feed gas, and the solid grey lines indicate the CH_4/CO_2 ratio in the vapor phase at the end of the hydrate formation at t_2 . (A) feed gas methane fraction 0.701, (B) feed gas methane fraction 0.503 and (C) feed gas methane fraction 0.285.

Figure 8 shows that at early times of the hydrate formation period, $\left(\frac{n_{\text{CH}_4}^H}{n_{\text{CO}_2}^H}\right)$ starts with small values and later accommodates to a plateau or a marginal linear increase. This means that, initially,

it is mainly CO₂ that acts as a guest molecule, while with increasing time CH₄ is also consumed for hydrate formation. For all experiments studied, the ratio of CH₄ to CO₂ in the hydrate phase at t_2 is in between the ratios measured in the vapor phase and the one measured in the liquid water-rich

phase: $\overline{\left(\frac{n_{\text{CH}_4}^{\text{L}}}{n_{\text{CO}_2}^{\text{L}}}\right)} < \overline{\left(\frac{n_{\text{CH}_4}^{\text{H}}}{n_{\text{CO}_2}^{\text{H}}}\right)} < \overline{\left(\frac{n_{\text{CH}_4}^{\text{V}}}{n_{\text{CO}_2}^{\text{V}}}\right)}$. Within the first 10 h of the hydrate formation period, some data rows seem to feature a maximum $\overline{\left(\frac{n_{\text{CH}_4}^{\text{H}}}{n_{\text{CO}_2}^{\text{H}}}\right)}$. Unfortunately, these maxima also fall into the regions in which the data points feature rather large error bars. Therefore, their existence can either be justified by a lack in the precision of the measurements made, or their existence might be explained by the circumstance that small hydrate cages (5¹²) in the sI hydrate structure, which prefer CH₄ molecules, are more likely to form at the initial stage of the hydrate formation. Both, previously reported experimental studies [42–44] and molecular dynamics simulation studies [45] support this theory. Note that CO₂ molecules are not suitable for encaging into the small cavities of sI hydrate because of the molecular size constraint [29]. The peak visible in Run 2 in Figure 8.A between 10 h and 15 h can be explained by a vapor phase bubble that was entrained into the hydrate gel. Still the peak maximum is smaller than the ratio $\overline{\left(\frac{n_{\text{CH}_4}^{\text{V}}}{n_{\text{CO}_2}^{\text{V}}}\right)}$ of the corresponding vapor phase ratio at similar times.

3.5. Determination of the Selectivity Factor

The selectivity factor of CO₂ (SF_{CO_2}) with respect to methane for the liquid water-rich phase at the end of the dissolution period at t_1 or for the solid hydrate phase at the end of the hydrate formation period at t_2 for three initial gas compositions is defined as

$$SF_{\text{CO}_2}^i = \frac{\left(\frac{n_{\text{CO}_2}^i}{n_{\text{CH}_4}^i}\right)}{\left(\frac{n_{\text{CO}_2}^{\text{V}}}{n_{\text{CH}_4}^{\text{V}}}\right)} = \frac{\frac{1}{\left(\frac{n_{\text{CH}_4}^i}{n_{\text{CO}_2}^i}\right)}}{\frac{1}{\left(\frac{n_{\text{CH}_4}^{\text{V}}}{n_{\text{CO}_2}^{\text{V}}}\right)}} \quad (8)$$

where the superscript i could be either L or H, which denotes the liquid water-rich phase or the pure solid hydrate phase, respectively. Selectivity factor of CO₂ $SF_{\text{CO}_2}^{\text{L}}$ for the liquid water-rich phase just before t_1 are determined as 29.27, 33.72, and 33.2 for the initial molar CH₄-fractions in the feed gas of 0.701, 0.503, and 0.285, respectively. Similarly, $SF_{\text{CO}_2}^{\text{H}}$ for the solid hydrate phase are 2.70, 2.81, and 2.86, respectively. The results show that $SF_{\text{CO}_2}^{\text{H}}$ is almost the same despite varying the initial gas compositions. Moreover, $SF_{\text{CO}_2}^{\text{L}}$ is larger than $SF_{\text{CO}_2}^{\text{H}}$ at each initial gas composition.

The selectivity factor of CO₂ ($SF_{\text{CO}_2}^{\text{G}}$) for the hydrate gel phase, including the CO₂ dissolved in the liquid-water-rich phase and the CO₂ captured in the solid hydrate, was calculated using the conventional method based on the amount of gas consumed for the entire reaction process. The detailed description of this method can be found elsewhere in previous studies [41,46]. The gas compositions at t_2 in the vapor phase used in the calculation could be converted from the mole ratios taken from the data shown in Figure 5. $SF_{\text{CO}_2}^{\text{G}}$ for the hydrate gel phase at t_2 are determined as 6.4, 8.1, and 8.2 for the initial molar CH₄-fractions in the feed gas of 0.701, 0.503, and 0.285, respectively. These values are in agreement with those reported by Di Profio et al. [41] from 3.1 to 7.1 and Zhong et al. [46] from 6.5 to 11.2. Also the selectivity factor of CO₂ (SF_{CO_2}) follows the order $SF_{\text{CO}_2}^{\text{H}} < SF_{\text{CO}_2}^{\text{G}} < SF_{\text{CO}_2}^{\text{L}}$. Therefore, it seems that the selectivity factor of CO₂ for hydrate might be overestimated in previous studies with the gas consumption method, if one considered using $SF_{\text{CO}_2}^{\text{G}}$ instead of $SF_{\text{CO}_2}^{\text{H}}$ to judge the performance of a separation process by forming hydrate.

4. Conclusions

Within this study we investigated into the suitability of a gas hydrate formation process for the separation of CH₄ and CO₂ from a feed gas or at least for the purification of one of the two compounds. One of the main findings of this study is that the main separation is achieved not by hydrate formation but by the preferential absorption of CO₂ into the liquid water-rich phase before the onset of hydrate formation. Also the hydrate phase preferentially (with respect to the vapor phase composition) incorporates CO₂, and therefore in principle could contribute to a further purification of CH₄ in the remaining vapor phase. But as the fraction of liquid water converted into solid hydrate is rather small with less than 30 mol%, the separation achieved by hydrate formation is small compared to the separation achieved by absorption. This can become significantly different, if more solid hydrate is formed. More solid hydrate can be formed if for example a more efficient mixing between the vapor and the gel phase is assured or if either the liquid water-rich phase is atomized through the vapor phase or the vapor phase is dispersed through the continuous liquid water-rich phase.

Author Contributions: Conceptualization, Z.L., C.C.H., and A.S.B.; data curation and analysis, Z.L. and C.C.H.; writing—original draft preparation, Z.L.; writing—review and editing, A.S.B.; supervision, C.C.H. and A.S.B.; funding acquisition, A.S.B. All authors have read and agreed to the published version of the manuscript.

Funding: The project leading to this contribution has received funding from the European Union’s Horizon 2020 research and innovation programme under ERC Starting Grant agreement No. 637654 (Inhomogeneities). The authors also gratefully acknowledge the funding from China Scholarship Council (Grant No. 201806050175) for supporting the visit of Zheng Li at TU Bergakademie Freiberg.

Conflicts of Interest: The authors declare no competing financial interest.

References

1. Sloan, E.D. Fundamental principles and applications of natural gas hydrates. *Nature* **2003**, *426*, 353–359. [[CrossRef](#)] [[PubMed](#)]
2. Englezos, P. Clathrate hydrates. *Ind. Eng. Chem. Res.* **1993**, *32*, 1251–1274. [[CrossRef](#)]
3. Ripmeester, J.A.; Tse, J.S.; Ratcliffe, C.I.; Powell, B.M. A new clathrate hydrate structure. *Nature* **1987**, *325*, 135–136. [[CrossRef](#)]
4. Ripmeester, J.A.; Alavi, S. Some current challenges in clathrate hydrate science: Nucleation, decomposition and the memory effect. *Curr. Opin. Solid State Mater. Sci.* **2016**, *20*, 344–351. [[CrossRef](#)]
5. Yin, Z.; Huang, L.; Linga, P. Effect of wellbore design on the production behaviour of methane hydrate-bearing sediments induced by depressurization. *Appl. Energy* **2019**, *254*, 113635. [[CrossRef](#)]
6. Li, X.S.; Xu, C.G.; Zhang, Y.; Ruan, X.K.; Li, G.; Wang, Y. Investigation into gas production from natural gas hydrate: A review. *Appl. Energy* **2016**, *172*, 286–322. [[CrossRef](#)]
7. Zheng, J.; Loganathan, N.K.; Zhao, J.; Linga, P. Clathrate hydrate formation of CO₂/CH₄ mixture at room temperature: Application to direct transport of CO₂-containing natural gas. *Appl. Energy* **2019**, *249*, 190–203. [[CrossRef](#)]
8. Wang, F.; Song, Y.-M.; Liu, G.Q.; Guo, G.; Luo, S.J.; Guo, R.-B. Rapid methane hydrate formation promoted by Ag&SDS-coated nanospheres for energy storage. *Appl. Energy* **2018**, *213*, 227–234.
9. Seo, S.D.; Hong, S.Y.; Sum, A.K.; Lee, K.H.; Lee, J.D.; Lee, B.R. Thermodynamic and kinetic analysis of gas hydrates for desalination of saturated salinity water. *Chem. Eng. J.* **2019**, *370*, 980–987. [[CrossRef](#)]
10. Dong, H.; Zhang, L.; Ling, Z.; Zhao, J.; Song, Y. The Controlling Factors and Ion Exclusion Mechanism of Hydrate-Based Pollutant Removal. *ACS Sustain. Chem. Eng.* **2019**, *7*, 7932–7940. [[CrossRef](#)]
11. Zhong, D.L.; Englezos, P. Methane Separation from Coal Mine Methane Gas by Tetra-n-butyl Ammonium Bromide Semiclathrate Hydrate Formation. *Energy Fuels* **2012**, *26*, 2098–2106. [[CrossRef](#)]
12. Cai, J.; Zhang, Y.; Xu, C.G.; Xia, Z.M.; Chen, Z.Y.; Li, X.S. Raman spectroscopic studies on carbon dioxide separation from fuel gas via clathrate hydrate in the presence of tetrahydrofuran. *Appl. Energy* **2018**, *214*, 92–102. [[CrossRef](#)]
13. Chazallon, B.; Pirim, C. Selectivity and CO₂ capture efficiency in CO₂-N₂ clathrate hydrates investigated by in-situ Raman spectroscopy. *Chem. Eng. J.* **2018**, *342*, 171–183. [[CrossRef](#)]

14. Lee, D.; Go, W.; Seo, Y. Experimental and computational investigation of methane hydrate inhibition in the presence of amino acids and ionic liquids. *Energy* **2019**, *182*, 632–640. [\[CrossRef\]](#)
15. Zerpa, L.E.; Salager, J.L.; Koh, C.A.; Sloan, E.D.; Sum, A.K. Surface Chemistry and Gas Hydrates in Flow Assurance. *Ind. Eng. Chem. Res.* **2011**, *50*, 188–197. [\[CrossRef\]](#)
16. Van Denderen, M.; Ineke, E.; Golombok, M. CO₂ Removal from Contaminated Natural Gas Mixtures by Hydrate Formation. *Ind. Eng. Chem. Res.* **2009**, *48*, 5802–5807. [\[CrossRef\]](#)
17. Ricaurte, M.; Dicharry, C.; Broseta, D.; Renaud, X.; Torre, J.-P. CO₂ Removal from a CO₂-CH₄ Gas Mixture by Clathrate Hydrate Formation Using THF and SDS as Water-Soluble Hydrate Promoters. *Ind. Eng. Chem. Res.* **2013**, *52*, 899–910. [\[CrossRef\]](#)
18. Li, Z.; Zhong, D.L.; Lu, Y.Y.; Yan, J.; Zou, Z.L. Preferential enclathration of CO₂ into tetra-*n*-butyl phosphonium bromide semiclathrate hydrate in moderate operating conditions: Application for CO₂ capture from shale gas. *Appl. Energy* **2017**, *199*, 370–381. [\[CrossRef\]](#)
19. Liu, J.; Ding, J.X.; Liang, D.Q. Experimental study on hydrate-based gas separation of mixed CH₄/CO₂ using unstable ice in a silica gel bed. *Energy* **2018**, *157*, 54–64. [\[CrossRef\]](#)
20. Lim, J.; Choi, W.; Mok, J.; Seo, Y. Clathrate-Based CO₂ Capture from CO₂-Rich Natural Gas and Biogas. *ACS Sustain. Chem. Eng.* **2018**, *6*, 5627–5635. [\[CrossRef\]](#)
21. Xia, Z.M.; Li, X.S.; Chen, Z.Y.; Li, G.; Yan, K.F.; Xu, C.G.; Lv, Q.N.; Cai, J. Hydrate-based CO₂ capture and CH₄ purification from simulated biogas with synergic additives based on gas solvent. *Appl. Energy* **2016**, *162*, 1153–1159. [\[CrossRef\]](#)
22. Lim, J.; Choi, W.; Mok, J.; Seo, Y. Kinetic CO₂ selectivity in clathrate-based CO₂ capture for upgrading CO₂-rich natural gas and biogas. *Chem. Eng. J.* **2019**, *369*, 686–693. [\[CrossRef\]](#)
23. Yue, G.; Liu, Y.; Luo, Y.; Liu, A.X.; Chen, B.; Sun, Q.; Li, X.X.; Dong, B.; Yang, L.Y.; Guo, X.Q. Combining Different Additives with TBAB on CO₂ Capture and CH₄ Purification from Simulated Biogas Using Hydration Method. *J. Chem. Eng. Data* **2019**, *64*, 1622–1631. [\[CrossRef\]](#)
24. Holzammer, C.C.; Braeuer, A.S. Raman Spectroscopic Study of the Effect of Aqueous Salt Solutions on the Inhibition of Carbon Dioxide Gas Hydrates. *J. Phys. Chem. B* **2019**, *123*, 2354–2361. [\[CrossRef\]](#)
25. Holzammer, C.; Schicks, J.M.; Will, S.; Braeuer, A.S. Influence of Sodium Chloride on the Formation and Dissociation Behavior of CO₂ Gas Hydrates. *J. Phys. Chem. B* **2017**, *121*, 8330–8337. [\[CrossRef\]](#)
26. Braeuer, A.; Hankel, R.F.; Mehnert, M.K.; Schuster, J.J.; Will, S. A Raman technique applicable for the analysis of the working principle of promoters and inhibitors of gas hydrate formation. *J. Raman Spectrosc.* **2015**, *46*, 1145–1149. [\[CrossRef\]](#)
27. Qin, J.; Kuhs, W.F. Quantitative analysis of gas hydrates using Raman spectroscopy. *AIChE J.* **2013**, *59*, 2155–2167. [\[CrossRef\]](#)
28. Braeuer, A. *In Situ Spectroscopic Techniques at High Pressure*; Elsevier Science: Amsterdam, The Netherlands, 2015.
29. Sloan, E.D.; Koh, C.A. *Clathrate Hydrates of Natural Gases*, 3rd ed.; CRC Press: Boca Raton, FL, USA, 2008.
30. Kumar, R.; Lang, S.; Englezos, P.; Ripmeester, J. Application of the ATR-IR Spectroscopic Technique to the Characterization of Hydrates Formed by CO₂, CO₂/H₂ and CO₂/H₂/C₃H₈. *J. Phys. Chem. A* **2009**, *113*, 6308–6313. [\[CrossRef\]](#)
31. Uchida, T.; Hirano, T.; Ebinuma, T.; Narita, H.; Gohara, K.; Mae, S.; Matsumoto, R. Raman spectroscopic determination of hydration number of methane hydrates. *AIChE J.* **1999**, *45*, 2641–2645. [\[CrossRef\]](#)
32. Chen, L.; Lu, H.; Ripmeester, J.A. Raman spectroscopic study of CO₂ in hydrate cages. *Chem. Eng. Sci.* **2015**, *138*, 706–711. [\[CrossRef\]](#)
33. Carey, D.M.; Korenowski, G.M. Measurement of the Raman spectrum of liquid water. *J. Chem. Phys.* **1998**, *108*, 2669–2675. [\[CrossRef\]](#)
34. Ludwig, R. Water: From Clusters to the Bulk. *Angew. Chem. Int. Ed. Engl.* **2001**, *40*, 1808–1827. [\[CrossRef\]](#)
35. Holzammer, C.; Finckenstein, A.; Will, S.; Braeuer, A.S. How Sodium Chloride Salt Inhibits the Formation of CO₂ Gas Hydrates. *J. Phys. Chem. B* **2016**, *120*, 2452–2459. [\[CrossRef\]](#) [\[PubMed\]](#)
36. Schuster, J.J.; Will, S.; Leipertz, A.; Braeuer, A. Deconvolution of Raman spectra for the quantification of ternary high-pressure phase equilibria composed of carbon dioxide, water and organic solvent. *J. Raman Spectrosc.* **2014**, *45*, 246–252. [\[CrossRef\]](#)
37. Alsmeyer, F.; Koß, H.J.; Marquardt, W. Indirect Spectral Hard Modeling for the Analysis of Reactive and Interacting Mixtures. *Appl. Spectrosc.* **2004**, *58*, 975–985. [\[CrossRef\]](#)

38. Kriesten, E.; Mayer, D.; Alsmeyer, F.; Minnich, C.B.; Greiner, L.; Marquardt, W. Identification of unknown pure component spectra by indirect hard modeling. *Chemometr. Intell. Lab. Syst.* **2008**, *93*, 108–119. [[CrossRef](#)]
39. Adami, R.; Schuster, J.; Liparoti, S.; Reverchon, E.; Leipertz, A.; Braeuer, A. A Raman spectroscopic method for the determination of high pressure vapour liquid equilibria. *Fluid Phase Equilib.* **2013**, *360*, 265–273. [[CrossRef](#)]
40. Luther, S.K.; Schuster, J.J.; Leipertz, A.; Braeuer, A. Non-invasive quantification of phase equilibria of ternary mixtures composed of carbon dioxide, organic solvent and water. *J. Supercrit. Fluid.* **2013**, *84*, 146–154. [[CrossRef](#)]
41. Di Profio, P.; Canale, V.; D'Alessandro, N.; Germani, R.; Di Crescenzo, A.; Fontana, A. Separation of CO₂ and CH₄ from Biogas by Formation of Clathrate Hydrates: Importance of the Driving Force and Kinetic Promoters. *ACS Sustain. Chem. Eng.* **2017**, *5*, 1990–1997. [[CrossRef](#)]
42. Uchida, T.; Ikeda, I.Y.; Takeya, S.; Kamata, Y.; Ohmura, R.; Nagao, J.; Zatsepina, O.Y.; Buffett, B.A. Kinetics and stability of CH₄-CO₂ mixed gas hydrates during formation and long-term storage. *ChemPhysChem* **2005**, *6*, 646–654. [[CrossRef](#)]
43. Schicks, J.M.; Luzi-Helbing, M. Cage occupancy and structural changes during hydrate formation from initial stages to resulting hydrate phase. *Spectrochim. Acta A Mol. Biomol. Spectrosc.* **2013**, *115*, 528–536. [[CrossRef](#)] [[PubMed](#)]
44. Lang, F.; Servio, P. Bulk liquid and gas mole fraction measurements during hydrate growth for the CH₄ + CO₂ + H₂O system. *J. Chem. Thermodyn.* **2018**, *117*, 113–118. [[CrossRef](#)]
45. He, Z.; Gupta, K.M.; Linga, P.; Jiang, J. Molecular Insights into the Nucleation and Growth of CH₄ and CO₂ Mixed Hydrates from Microsecond Simulations. *J. Phys. Chem. C* **2016**, *120*, 25225–25236. [[CrossRef](#)]
46. Zhong, D.L.; Li, Z.; Lu, Y.Y.; Wang, J.L.; Yan, J. Evaluation of CO₂ removal from a CO₂+CH₄ gas mixture using gas hydrate formation in liquid water and THF solutions. *Appl. Energy* **2015**, *158*, 133–141. [[CrossRef](#)]



© 2020 by the authors. Licensee MDPI, Basel, Switzerland. This article is an open access article distributed under the terms and conditions of the Creative Commons Attribution (CC BY) license (<http://creativecommons.org/licenses/by/4.0/>).